Hopping trajectories due to long-range interactions determine surface accumulation of microalgae

Buchner, Abel John; Muller, Koen; Mehmood, Junaid; Tam, Daniel

DOI
10.1073/pnas.2102095118

Publication date
2021

Document Version
Final published version

Published in
Proceedings of the National Academy of Sciences of the United States of America

Citation (APA)
Buchner, A. J., Muller, K., Mehmood, J., & Tam, D. (2021). Hopping trajectories due to long-range interactions determine surface accumulation of microalgae. *Proceedings of the National Academy of Sciences of the United States of America*, *118*(20), Article e2102095118. https://doi.org/10.1073/pnas.2102095118

Hopping trajectories due to long-range interactions determine surface accumulation of microalgae

Abel-John Buchner[a], Koen Muller[a], Junaid Mehmood[a], and Daniel Tam[a,1]

[a]Faculty of Mechanical, Maritime, and Materials Engineering, Delft University of Technology, 2628 CD Delft, the Netherlands

Edited by David A. Weitz, Harvard University, Cambridge, MA, and approved April 10, 2021 (received for review February 2, 2021)

The accumulation of motile cells at solid interfaces increases the rate of surface encounters and the likelihood of surface attachment, leading to surface colonization and biofilm formation. The cell density distribution in the vicinity of a physical boundary is influenced by the interactions between the microswimmers and their physical environment, including hydrodynamic and steric interactions, as well as by stochastic effects. Disentangling the contributions of these effects remains an experimental challenge. Here, we use a custom-made four-camera view microscope to track a population of motile puller-type *Chlamydomonas reinhardtii* in a relatively unconstrained three-dimensional (3D) domain. Our experiments yield an extensive sample of 3D trajectories including cell-surface encounters with a planar wall, from which we extract a full description of the dynamics and the stochasticity of swimming cells. We use this large data sample and combine it with Monte Carlo simulations to determine the link between the dynamics at the single-cell level and the cell density. Our experiments demonstrate that the near-wall scattering is bimodal, corresponding to steric and hydrodynamic effects. We find, however, that this near-wall dynamics has little influence on the cell accumulation at the surface. On the other hand, we present evidence of a cell-induced surface-directed rotation leading to a vertical orbiting behavior and hopping trajectories, consistent with long-range hydrodynamic effects. We identify this long-range effect to be at the origin of the significant surface accumulation of cells.

microswimmers | surface accumulation | 3D tracking | stochastic simulations

The physical interactions of single-celled organisms with their surroundings have many ecological, medical, and technological implications (1–3). Interactions of planktonic algae or bacteria with solid substrates modulate the population distribution (4, 5), consequentially affecting the processes of surface attachment, colonization, and biofilm growth (6, 7). Elucidating the mechanisms governing these interactions is paramount to technological advances in biofouling prevention (8), to the development of cell manipulation strategies (9, 10), and to our understanding of microbial colonization and infections (11).

Physical mechanisms, suggested to influence cell-surface interactions and accumulation, include hydrodynamic interactions (12, 13), steric interactions and wall scattering (14–16), stochastic processes (17), and flow (18). The contributions of each of these mechanisms have been investigated in previous theoretical work. These studies have highlighted the role of hydrodynamic interactions in the scattering of both "pusher"- and "puller"-type motile cells at a no-slip solid surface (19–22). For pusher-type cells, steric interactions and stochastic processes have been shown theoretically to be sufficient to account for the surface accumulation of cells at the solid interface (14, 15).

Experimental studies of motile bacteria have linked hydrodynamic interactions with solid surfaces to wall trapping (13), to variations in the swimming speed (3), in the orientation relative to the surface (12), and in the orientation in the surface-parallel plane (23). Studies of puller organism *Chlamydomonas reinhardtii* have focused on the near-wall scattering dynamics. In shallow flow chambers, steric contact has been suggested to dominate surface interactions (10), while effects of hydrodynamic interactions have been evidenced in interactions with curved surfaces (24). Visualization and tracking constraints have often limited experimental studies of flagellates to two-dimensional (2D) flow cells (10, 24–26). Such confinement restricts the motion of the microorganisms in one dimension and alters the flow and the hydrodynamic effects compared with the dynamics of unconstrained swimmers interacting with an infinite planar wall predicted by theoretical studies (12, 19–21).

Here, we use a custom-made multiview microscope to track the unconstrained three-dimensional (3D) dynamics of *C. reinhardtii* interacting with planar surfaces. Previous 3D tracking experiments have been limited to single cells (27, 28) or small populations at very low density (29). Recent experiments using holography (30–33) have required low optical densities and relatively small measurement domains (34, 35). In addition, holographic measurements have a limited accuracy along the optical axis (36), which hinders the resolution of contact and noncontact cell wall interactions. Our experimental setup circumvents these limitations by using four cameras recording at four different angles to reconstruct the 3D dynamics and trajectories of a large population of cells, within a flow cell of dimension $h = 2$ mm along the optical axis and within a position error smaller than the cell radius. Close to the wall, our measurement

Significance

How motile cells accumulate on solid surfaces is of crucial importance to phenomena, such as surface colonization, biofilm formation, and biofouling, with biological, medical, ecological, and industrial implications. Cell accumulation and adhesion to a substrate are influenced by different mechanical and physical interactions, including hydrodynamic and steric interactions. Determining their relative contributions to the increase in cell density at solid surfaces is experimentally challenging. Here, a unique multicamera three-dimensional experimental measurement reveals the existence of long-range interactions between green algae *Chlamydomonas reinhardtii* cells and surfaces, which are directly responsible for the increase of cell density near surfaces. It is our hope that these results will contribute to the design of surfaces to modulate, promote, and inhibit surface adhesion.

Author contributions: A.-J.B., K.M., and D.T. designed research; A.-J.B. and J.M. performed research; A.-J.B. analyzed data; K.M. developed the cell-tracking algorithm; and A.-J.B. and D.T. wrote the paper.

The authors declare no competing interest.

This article is a PNAS Direct Submission.

[1]To whom correspondence may be addressed. Email: d.s.w.tam@tudelft.nl.

This article contains supporting information online at https://www.pnas.org/lookup/suppl/doi:10.1073/pnas.2102095118/-/DCSupplemental.

Published May 12, 2021.

method resolves a bimodal distribution corresponding to contact and noncontact wall scattering interactions. Away from the wall, we report a long-range attraction effect leading to hopping trajectories and repeated surface approaches. The cell density distribution measured in the flow cell is compared with results from Monte Carlo simulations, which reveal that long-range interactions drive the surface population accumulation, not the detail of the contact/noncontact near-wall interactions.

Experimental Approach

We recorded the 3D dynamics of individual cells, in a dilute suspension of density $\rho = 2 \times 10^4$cells per mL, of the common model motile organism, the biflagellated green alga *C. reinhardtii* (37). The motility of the cell originates in the "breaststroke" motion of its two anterior flagella of length l_f resulting in an average swimming velocity U. In our experiments, we measured $l_f \approx 10\mu m$, $U \approx 100\mu$m/s, and cell body diameter, $D \approx 10\mu m$, in agreement with previous motility studies of *C. reinhardtii* (25, 37–40), see *SI Appendix*, Fig. S1 for details.

Suspensions of *C. reinhardtii* were loaded inside a flow chamber between two parallel glass coverslips, treated to prevent cell-surface adhesion (*Materials and Methods*). The distance between the two planar glass surfaces corresponded to the smallest dimension of the flow cell $H = 2\,\text{mm} \approx 200D$. The geometry of the flow cell allows us to observe the interactions between motile cells and the planar surfaces of the glass coverslips in an unconstrained 3D fluid environment. The suspensions were illuminated using a light source (Luminus; PT-120-TE) at intensity $100\mu mol/m^2$s. The wavelength of the illumination was $\langle\lambda\rangle = 613$nm, beyond the phototactic action spectrum of *C. reinhardtii* (37, 41–43), to avoid inducing a phototactic response. Experiments were performed at an ambient temperature of $T \approx 25^\circ$C.

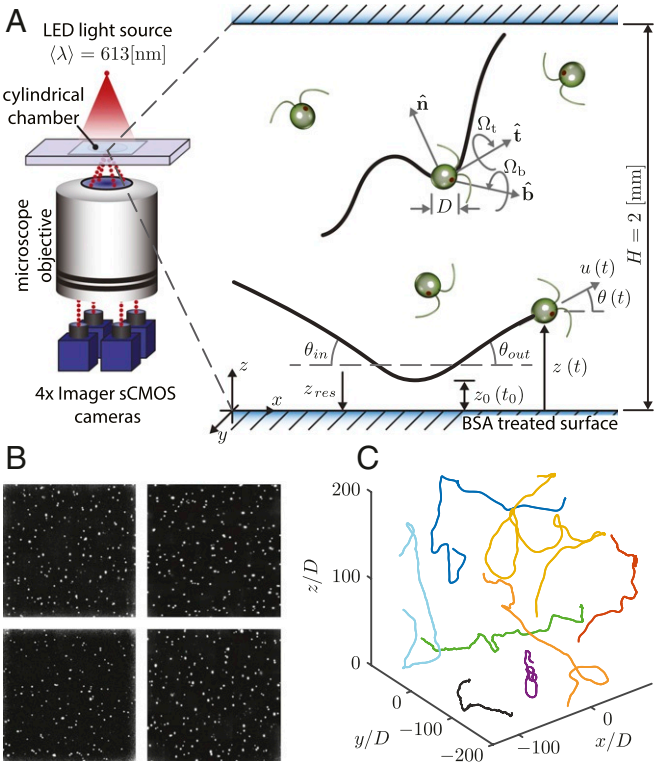

Fig. 1. (*A*) Schematic representation of the key elements of the experimental apparatus. A cylindrical fluidic domain containing a suspension of *C. reinhardtii* is illuminated at $\langle\lambda\rangle = 613$nm. Four Imager sCMOS cameras (LaVision) view the fluidic domain off center through a single objective lens (Zeiss). The minimum dimension of the measurement domain, from surface to surface, is H = 2 mm. Coordinate systems and nomenclature used throughout the paper are given in the enlarged schematic view of the measurement domain. BSA, bovine serum albumin. (*B*) Example images from each camera of cells at suspension density $\rho = 2 \times 10^4$ cells per mL. (*C*) Sample of reconstructed 3D cell trajectories.

We used a custom-built multicamera microscopy setup to image a dilute suspension (Fig. 1). Videographic data were recorded simultaneously from four LaVision Imager sCMOS cameras at 20Hz (exposure time 42ms). The optical viewing path of each camera passed through a single large objective (Zeiss; $M = 1.50$, $f^{\#} = 15$), offset from the objective axis such that all cameras viewed a common measurement domain but from viewing directions separated by approximately 20° (44, 45). The camera aperture was set such that the entire height of the 2-mm flow chamber was in focus (*Materials and Methods* has details).

We first tracked the cells in the image plane of each camera view. These tracked objects were then matched between camera views and triangulated to find the 3D spatial coordinates $\mathbf{X} = (x(t), y(t), z(t))$ using a custom-made tracking algorithm similar to ref. 46 (*Materials and Methods*). The average skewness error (47) in this triangulation was $\epsilon = 3.7 \pm 1.7\mu m$ $(0.37 \pm 0.17D)$, which compares favorably with typical particle location uncertainty of 1 to 2 cell diameters using holographic methods (36). The tangential vector, $\hat{\mathbf{t}}$, is defined in relation to the velocity of each track as $\mathbf{u}(t) = U\hat{\mathbf{t}}(t)$. The xy plane corresponds to the planar glass surface. We define as $\theta(t)$ the angle between the cell velocity vector, $\mathbf{u}(t)$, and the xy plane of the surface. Only tracks longer than 1 s, with median velocity $60 \leq |\tilde{\mathbf{u}}(t)| \leq 140\mu$m/s, are considered here. Our experiment yields $N = 16469$ such tracks, the statistics of which are sufficient to reveal both near-surface scattering behavior and subtle effects in the far field.

Near-Surface Interactions and Scattering

First, we investigate the scattering dynamics of motile cells in the near-surface region, by only considering the trajectories approaching the surface within a distance of $z_{\text{res}} = 30\mu m$. We use our large data sample to characterize the scattering mechanisms from the kinematics of the cells and determine the importance of steric and hydrodynamic effects. For each of the $N = 1421$ trajectories in the "near-surface" region, we define $x_{2D}(t)$ as the distance traveled in the surface-parallel xy plane and report the cell trajectories $(x_{2D}(t), z(t))$ near the surface. We call t_0 the time at which the cell is at a minimum distance $z(t_0) = z_0$ from the surface. Fig. 2*A* represents the distribution of these trajectories in (x_{2D}, z) coordinates deduced from all N trajectories recentered at the position of minimal approach to the surface $x_{2D}(t_0)$. The residence time τ_{res}, for which a cell resides in the near-surface region $z(t) \leq z_{\text{res}}$, scales inversely with the median swimming speed of the cell (*SI Appendix*, Fig. S2). The short residence time, $\tau_{\text{res}} \sim \mathcal{O}(1)$s, indicates that long-period trapping is minimal. This provides support for a deterministic departure mechanism, such as the combination of cell rotation and flagellar contact proposed by refs. 21 and 24, rather than the entrapment and noise-mediated release observed for other swimmer geometries (48).

Steric interactions with the wall have been evidenced to play an important role in the scattering dynamics of ciliates (10). It is reasonable to assume that such direct contact interactions may be characterized by stronger fluctuations in the velocity and the swimming direction, as the cilia come in sudden contact with the wall, leading to changes in the cell velocity and orientation. To identify such interactions and quantify their prevalence in our experiments, we consider the rate of change of the pitch angle $\theta(t)$ relative to the surface, as well as the rate of change of the swimming velocity $U(t)$. Fig. 2 *B* and *C* represents the distribution for the pitching rate $\dot{\theta}$ and the tangential acceleration $\dot{U}$,

both given as a function of time. Fig. 2*B* shows a short positive increase of $\dot{\theta}$ around the time of closest approach t_0, corresponding to a brief cell rotation away from the surface and consistent with surface scattering. Fig. 2*C* highlights another signature of wall interaction in the fluctuations of $U(t)$, with a reduction in swimming velocity before t_0, followed by reacceleration to the original velocity after t_0.

Close inspection of the distribution of $\dot{U}$ reveals, however, that many (x_{2D}, z) trajectories are not characterized by an abrupt deceleration and acceleration at the surface. Rather, for many trajectories, scattering occurs at a constant velocity (Fig. 2*C*). These differences in scattering dynamics can be identified on the joint probability density function for the peak values of $\dot{\theta}(t_0)$ and $\dot{U}(t_0 - 0.25\text{s})$ (Fig. 2*D*). This joint probability density function (PDF) reveals a bimodal distribution in the kinematics of the scattering trajectories. This indicates two distinct modes of cell-surface interactions, exhibiting qualitatively different scattering behavior. The first mode is characterized by large fluctuations in the kinematics around the point of nearest approach, with $\dot{\theta}D/U = 0.42$ and $\dot{U}/U = -0.11$ (contact mode [C mode] in Fig. 2*D*). The second mode includes trajectories with near-constant velocity scattering peak at $\dot{\theta}D/U = 0.15$ and small pitching rate $\dot{U}/U = -0.01$ (noncontact mode [NC mode] in Fig. 2*D*).

The impulsive kinematics of trajectories within the C mode bear the signature of close contact interaction with the surface. Hence, we proceed by considering the distribution of minimal approach distance z_0 for the C and NC modes separately. For this, we fit a 2D Gaussian distribution to each peak (Fig. 2*D*) to distinguish the trajectories within each scattering mode. For the C mode, the distribution of z_0 is maximum for $z_0 \leq 15\ \mu m$ and rapidly decreases to zero at larger distances from the surface (Fig. 2*E*). For the NC mode, on the other hand, the distribution of z_0 is small in the vicinity of the solid surface and rapidly increases for $z_0 > 15\ \mu m$. Given the average cell diameter, $D \approx 10\ \mu m$, and length of the anterior flagella of *C. reinhardtii*, $l_f \approx 10\ \mu m$, we confirm that for the trajectories within the impulsive C mode, the cells have come in direct contact with the wall. From the distribution of closest approach distances z_0, we can conclude that within the continuous NC mode, cells have scattered from the wall without direct contact with the solid interface and suggest a scattering due to hydrodynamic interactions.

Fig. 2 *F* and *I* represents the distribution and average of all (x_{2D}, z) trajectories in the C and NC modes, respectively. The scattering trajectories in both modes are strikingly different. Within the C mode, trajectories are asymmetric with cells approaching the wall over a range of predominantly steep angles and departing predominantly at shallow angles (Fig. 2*F*). Within the NC mode, the trajectories are symmetric, and both the approach and departure angles are much smaller than in the C mode (Fig. 2*I*). These results are in agreement with previous theoretical work by Spagnolie and Lauga (19). We define, for each trajectory, the approach angle θ_{in} and the departure angle θ_{out} (Fig. 1) and represent the joint probability distribution of $(\theta_{\text{in}}, \theta_{\text{out}})$ for the C and NC modes in Fig. 2 *G* and *J*, respectively. Contact interactions occur for a range of steep θ_{in} and depart at a shallower θ_{out} angle. The angle θ_{out} is independent of θ_{in} (black line in Fig. 2*G*), therefore defining a critical departure angle of $\theta_{crit} \sim \mathcal{O}(20°)$, consistent with previous experimental work (10). By contrast, noncontact interactions occur for shallow approach angles, which are smaller than the critical departure angle $\theta_{in} < \theta_{crit}$. In addition, the scattering trajectories are symmetric, such that the distribution follows the line $\theta_{\text{out}} = \theta_{\text{in}}$ (Fig. 2*J*). Our experimental observations are in qualitative agreement with theoretical work by Spagnolie and Lauga

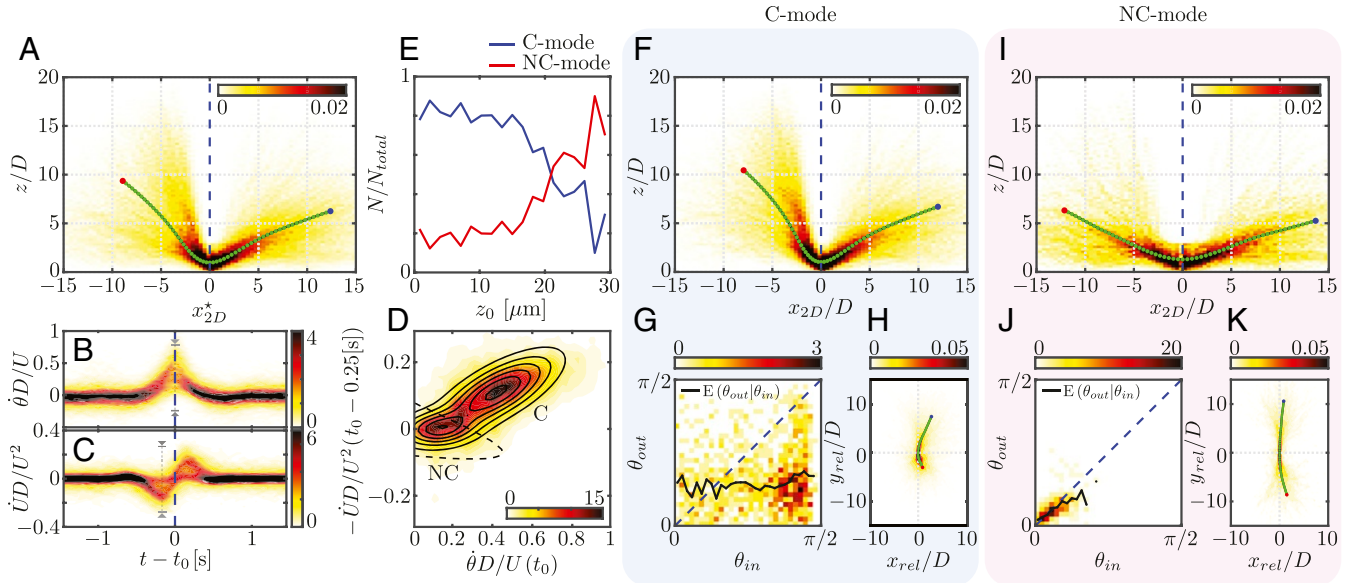

Fig. 2. (*A*) Distribution of cell trajectories in (x_{2D}, z) coordinates within $t_0 \pm 1.5$s of a close surface encounter. Green markers indicate the mean trajectory, with motion from the red marker toward blue. The vertical blue dashed line indicates the moment of closest approach, t_0. (*B* and *C*) Evolution of PDFs of pitching rate, $\dot{\theta}$, and tangential acceleration, $\dot{U}$, through all close surface approaches. The gray dashed lines in *B* and *C* correspond to the times at which the peak values are obtained, which we use to construct the joint PDF in *D*. (*D*) Joint PDF of pitching rate, $\dot{\theta}$, at $t = t_0$ and tangential acceleration, $\dot{U}$, at $t = t_0 - 0.25$s. The 2D Gaussian distributions fitted to the two peaks of the observed bimodal distribution are indicated by black contours. The dashed black curve delineates $G_C/G_{NC} = 1$, which we use as a criterion for classifying individual trajectories into C-mode or NC-mode cell-surface interactions. (*E*) Distributions of closest approach distance for contact and noncontact interactions. (*F* and *I*) Similar to *A* for contact and noncontact interactions, respectively. (*G* and *J*) PDF of surface departure angle, θ_{out}, given approach angle, θ_{in}, for (*G*) contact and (*J*) noncontact events. The blue dashed line indicates $\theta_{\text{out}} = \theta_{\text{in}}$. The mean departure angle conditional on θ_{in} is indicated in each case by the solid black line. (*H* and *K*) For contact and noncontact events, respectively, joint PDFs of trajectory locations projected into the surface-parallel (x, y) plane and aligned into the coordinate system, (x_{rel}, y_{rel}), relative to the cell orientation at t_0.

(19). For sufficiently steep values of θ_{in}, hydrodynamic effects are insufficient to prevent surface contact (19), and cells leave the surface only after their orientation exceeds a critical angle, $\theta_{crit} \approx \mathcal{O}(22^\circ)$. Only for $\theta_{in} < \theta_{crit}$ do hydrodynamic forces prevent contact. The signatures of the trajectories projected in the xy plane of the solid surface also differ; contact interactions are characterized by the trajectories rapidly turning to the right (Fig. 2*H*), while for noncontact interactions, they remain mostly straight (Fig. 2*K*).

Long-Range Interactions and Vertical Hopping Behavior

We now characterize the swimming dynamics far from the surface and consider all $N = 16{,}469$ recorded cell trajectories within the 2-mm height of the flow chamber. We focus on wall interactions and report the dynamics along the wall normal z direction. The motion of a cell along the z axis is determined by the pitching rate $\dot{\theta}$ for a given pitch angle θ and position z in the flow chamber. By considering the pitch dynamics of the cells throughout the flow chamber, we identify regions of wall repulsion and attraction.

Fig. 3 presents our results for $\langle \dot{\theta} \rangle = f(z, \theta)$. The black dashed vertical line delineates downward ($\theta \leq 0$) and upward ($\theta \geq 0$) swimming cells.

We first consider the lower surface of the flow chamber at $z = 0$. Close to the surface, within $z < 30$ μm, $\langle \dot{\theta} \rangle$ is positive for all values of θ, corresponding to cells turning away from the surface and therefore, to surface repulsion. This is consistent with the surface scattering near the wall discussed previously (Fig. 2*B*). It is noteworthy that this repulsion region extends up to $z \approx 30$ μm and therefore, beyond the contact region (Fig. 3 *B* and *C*). This is further evidence for the existence of noncontact scattering. For $z > 30$ μm, the sign of the pitching rate changes, with $\langle \dot{\theta} \rangle \leq 0$ for a wide range of values of θ (Fig. 3 *A* and *B*). In this region, the swimming cells reorient toward the surface. This reorientation is strongest for cells swimming toward the surface $\theta < 0$ and weaker for cells swimming away from the surface with a small positive pitch angle θ. For large positive pitch angles, the pitching rate is negative, indicative of surface repulsion. At distances greater than $400 - 500$ μm, we find $\langle \dot{\theta} \rangle \approx 0$ such that the cells are neither attracted to nor repelled by the surface. The same pitching dynamic is observed on the top surface of the flow chamber at $z = 2{,}000 \mu$m, with similar magnitude and opposite signs for θ and $\langle \dot{\theta} \rangle$ (Fig. 3*A*). The hydrodynamic interaction of a dipole with a surface elicits a rotational response toward or away from the surface, depending on dipole orientation (12). Our experimental data indicate a corresponding behavior in *C. reinhardtii*. The key difference is a bias toward surface-directed rotation over rotation away from the surface. Cells oriented toward the surface exhibit rotation toward the surface, while the rotational response of cells oriented away from the surface is closer to neutral. We hypothesize that this difference is due to the front to back asymmetry of swimming *C. reinhardtii*.

The repulsion region for $z < 30$ μm and the attraction region for $z > 30$ μm suggest the existence of trajectories, moving periodically closer and away from the surface. We can verify the existence of these pseudoperiodic trajectories by integrating the first-order equation $\dot{z} = U \cdot \sin(\theta)$ using the empirical pitching map f in Fig. 3*A*. Such a trajectory is represented in black on Fig. 3*B*. The amplitude of the motion grows until it reaches a limit cycle of amplitude ~ 125 μm and period $\sim 8 - 10$s, where the cell periodically comes within a close distance to the wall. The robustness of our tracking method supports continuous tracking for long time periods, and we can therefore verify the existence of such hopping trajectories. Fig. 3*C* presents one such track in agreement with the attraction–repulsion cycles inferred by the pitching dynamics in (θ, z) coordinates. Several of such recorded trajectories are represented in the (x_{2D}, z) plane (Fig. 3*D*) and display the trajectories characterized by successive surface approaches.

Cell Distribution and Surface Accumulation

Following the characterization of cell-surface interactions, the outstanding questions are whether and how these surface interactions modulate the surface accumulation and the cell distribution (12, 14, 15). To address this question, we characterize the distribution of cells in our experimental chamber. Our experiments are performed at low cell concentration, such that we average the density distribution over the entire recording. Fig. 4 *A*, blue circles represents this time-averaged cell population density normalized by the bulk density. We find a statistical accumulation of *C. reinhardtii* at the surface and characterize the cell distribution with a penetration length $\delta_{exp} = \int_0^{1000} (\rho(z) - \rho_{bulk})/(\rho(0) - \rho_{bulk})\, dz = 73.8 \mu m$.

The extensive dataset gathered provides a full description of the different aspects of the swimming dynamics, including its stochastic nature. We use this data sample to implement Markov chain Monte Carlo (MCMC) simulations to reproduce the dynamics of the algae in the flow chamber. We take advantage of the MCMC simulations to disentangle the contributions of the different features of cell-surface interactions identified in our study and directly probe their effect on the cell population distribution. In particular, we first investigate the influence of the rotational diffusion, before including the effects of the near-wall scattering dynamics and later, the long-range vertical wall attraction behavior. We find that, in our experiments, the long-range behavior dictates the accumulation of cells at the interface.

Our approach integrates the stochastic dynamics for the cell position $\mathbf{X}(t + \Delta t) = \mathbf{X}(t) + |\mathbf{u_{cell}}| \hat{\mathbf{t}} \Delta t$ through time, assuming a constant swimming velocity of $|u_{cell}| = 100 \mu$m/s for simplicity (*Materials and Methods*). The tangent vector $\hat{\mathbf{t}}$, which characterizes the swimming direction, is evolved stochastically according to the empirical data collected in our experiments. We first consider the diffusive rotational behavior of the swimming cells, which we extract from the empirical data. For each trajectory recorded far from the surfaces, we define the tangent $\hat{\mathbf{t}}$, normal $\hat{\mathbf{n}}$, and binormal $\hat{\mathbf{b}}$ local unit vector in the Frenet–Serret frame (Fig. 1). In this frame of reference, we determine from the empirical data the conditional probability distributions of the rotation rates $\mathrm{P}(\Omega_t(t + \Delta t) | \Omega_t(t))$ and $\mathrm{P}(\Omega_b(t + \Delta t) | \Omega_b(t))$ (Fig. 4 *B* and *C*, respectively). In this framework, Ω_n about the normal vector $\hat{\mathbf{n}}$ is by definition zero. Rotation rates were drawn at each time step by sampling the corresponding inverse cumulative distributions (49). The resulting stochastic dynamics of the cells were integrated in time with a time step equal to the experimental time step, $\Delta t = 0.05$s.

Fig. 4*H* illustrates a representative trajectory obtained from these simulations, which is qualitatively similar to the experimentally measured trajectories. In addition, the time evolution of the mean square displacement (MSD) (Fig. 4*G*) of the experimentally measured cell position indicates a diffusive behavior, from which we can estimate the diffusion coefficient as $\mathcal{D} = (1.60 \pm 0.13) \times 10^{-8} m^2 s^{-1}$ and the characteristic diffusive timescale $\tau \sim \mathcal{D}/U^2 = 2.50 \pm 0.20$s. These measurements are in agreement with previously reported values (50). We obtain the identical diffusive behavior by computing the MSD from the solutions to the stochastic simulations, which validates our approach.

Near-surface accumulation has been shown to arise from a purely diffusive motion interacting with a planar no-slip surface (17). To investigate this, we simulated cells placed initially at random z locations and orientations. The trajectories were integrated until convergence to a final steady-state population

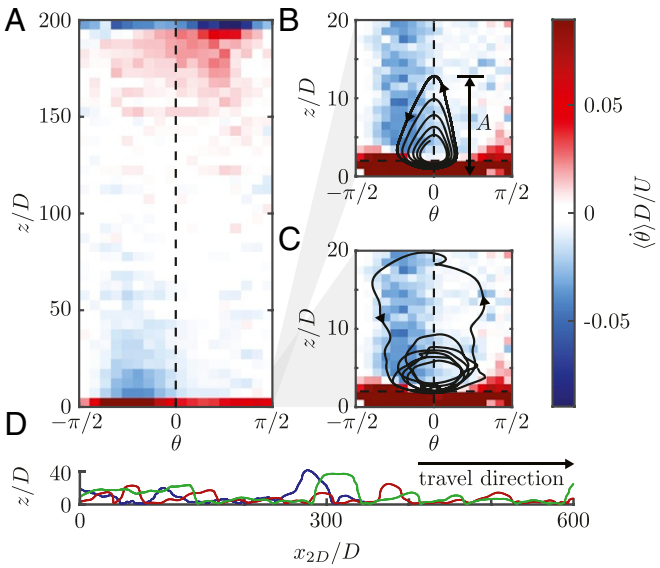

Fig. 3. (*A*) The mean value of cell pitching rate $\dot{\theta}$ conditional to the pitch angle θ and surface-normal coordinate z across the span of the experimental chamber. The vertical black dashed line indicates surface-parallel cell orientations. *B* and *C* provide expanded views of this state space in the near-surface region. A horizontal black dashed line delineates $z/D = 2$, within which cell-surface contact is possible. By integrating through this (θ, z) state space, the expected mean deterministic trajectory of a cell near a surface can be extracted. The example in *B* (black curve) begins at $(\theta, z/D) = (0, 5)$ with constant velocity magnitude of $U = 100\mu$m/s. A pseudoperiodic motion is observed, growing in amplitude before reaching a limit cycle of amplitude $A/D \approx 12.5$. An example of a measured trajectory displaying this orbiting behavior in $(\theta, z/D)$ coordinates is given in *C* (black curve). A sample of measured trajectories shown in *D* demonstrates the oscillations in the cell-surface separation distance, z, associated with this orbiting and leading to hopping trajectories in (x_{2D}, z) coordinates.

distribution (*SI Appendix*, Fig. S3). Interactions with the surface were modeled by assuming evenly distributed random scattering angles and an exponentially distributed residence time distribution with characteristic timescale, $\tau_s = 2.5$s, equal to the measured diffusive kinematics. Fig. 4*A* reports the resulting cell distribution (red crosses). The extent of surface accumulation agrees with that reported for the run-and-tumble simulations from ref. 17 (Fig. 4*A*). The penetration length scale of this cell distribution, $\delta = 32.2\mu m$, is however much shorter than the one extracted in our experiments, and therefore, the diffusive nature of the cell kinematics is not at the origin of the significant surface accumulation reported in our experiments.

Next, we investigate whether the near-wall scattering dynamics can account for this discrepancy. We do this by repeating the stochastic simulations but including the near-wall scattering dynamics observed in the experiments. For each encounter of a cell with a surface, the near-surface scattering parameters, τ_{res} and θ_{out}, are stochastically sampled from the empirically determined distributions $\mathrm{P}(\tau_{\mathrm{res}})$ and $\mathrm{P}(\theta_{\mathrm{out}})$ (Fig. 4 *E* and *F*). We find that the near-wall scattering dynamics does not significantly affect the cell distribution and does not account for the cell accumulation measured in the experiments (Fig. 4*A*).

At last, we study the effect of the long-range interactions described in Fig. 3. We include in our stochastic simulations the long-range effect on the pitching dynamics $\langle\dot{\theta}\rangle = f(z, \theta)$ in the evolution of the swimming direction $\hat{\mathbf{t}}$. At each time step, the surface-directed rotation rate, $\dot{\theta}(t)$, is selected via inverse transform sampling from the probability distribution, $\mathrm{P}(\dot{\theta}(t)|\theta, z)$, conditional on the instantaneous position of the cell in the state space presented in Fig. 3. This stochastically chosen rotation is added to the rotations, Ω_t and Ω_b, about the Lagrangian body frame. By including these long-range effects, our simulations yield trajectories characterized by successive surface approaches (Fig. 4*I*), which are similar to the trajectories recorded experimentally (Fig. 3*C*). The distribution of cell density for the simulations including the surface-directed rotation, $\dot{\theta}$, reveals a significant increase in cell accumulation at the wall, in agreement with experiments (Fig. 4*A*). The agreement between simulations and experiments is excellent. In particular, the penetration length of the computed distribution $\delta = 76.5\mu m$ compares well with our measurements. This applies generally regardless of the near-surface scattering applied (compare Fig. 4 *A*, green vs. red squares), indicating that long-range cell-surface interactions dominate over both diffusion and the near-surface scattering dynamics in determining the degree of population accumulation near a surface.

Discussion

We have investigated the interactions between *C. reinhardtii* and flat no-slip surfaces. In the near-wall region, we elucidate the characteristics of close cell-surface encounters and distinguish between two scattering modes, corresponding to cells that come in direct contact with the surface and cells that do not. For contact interactions, our experiments in a 3D fluidic domain confirm the surface departure angle to be in the range $\theta_{\mathrm{out}} \sim \mathcal{O}(20^\circ)$, as previously observed in quasi-2D experiments. The departure angle is found to be independent of the approach angle, θ_{in}, even for very shallow angles and supports the argument that this critical departure angle is determined by geometric considerations of the organism during contact (10, 24). While we find contact scattering to occur more often than noncontact scattering, we still observe frequent noncontact scattering with planar walls, accounting for a significant fraction of close ($z_0 < 30\ \mu$m) surface encounters. These noncontact interactions are characterized by the symmetry of the trajectories, which reflects the time reversibility of the Stokes equations, in qualitative agreement with theoretical studies of the hydrodynamics of cell-surface interactions (19). The near-wall scattering dynamics observed in our experiments differs from those observed in flow chambers confining the flow field generated by the microswimmers between two narrowly separated plates (10). This indicates that near-wall scattering is affected by the confinement of the flow. We also observe that *C. reinhardtii* circle near surfaces. Our analysis indicates that, unlike the circling exhibited by pusher-type bacterial cells (23), the circular motion of *C. reinhardtii* on surfaces is nonhydrodynamic in nature, with turning in the surface plane observed only when contact is made between cell and surface.

Away from the wall, for $z/D > 3 - 4$, *C. reinhardtii* cells swimming toward the wall, for $\theta < 0$, rotate toward the surface, which is consistent with long-range hydrodynamic interactions for puller-type microswimmers (12, 19, 21). For cells moving away from the surface, $\theta > 0$, far-field hydrodynamic theory indicates a repulsive reorientation. In contrast, we observed that although the trend of $\dot{\theta}$ in the (θ, z) state space matches that predicted by this theory, there is a strong bias toward surface-directed rotation. This bias induces cells leaving the surface to reorient toward the surface and explains our observations of hopping trajectories, characterized by periodic surface interactions. Qualitatively similar oscillatory attraction–repulsion limit cycles have previously been predicted to result from cell-surface hydrodynamic interactions using various theoretical swimmer models (e.g., refs. 51–53).

Using MCMC simulations, we establish the link between the dynamics of the motility near interfaces on the micrometer scale and the distribution of cells throughout the flow chamber on the millimeter scale. We conclude that the near-wall

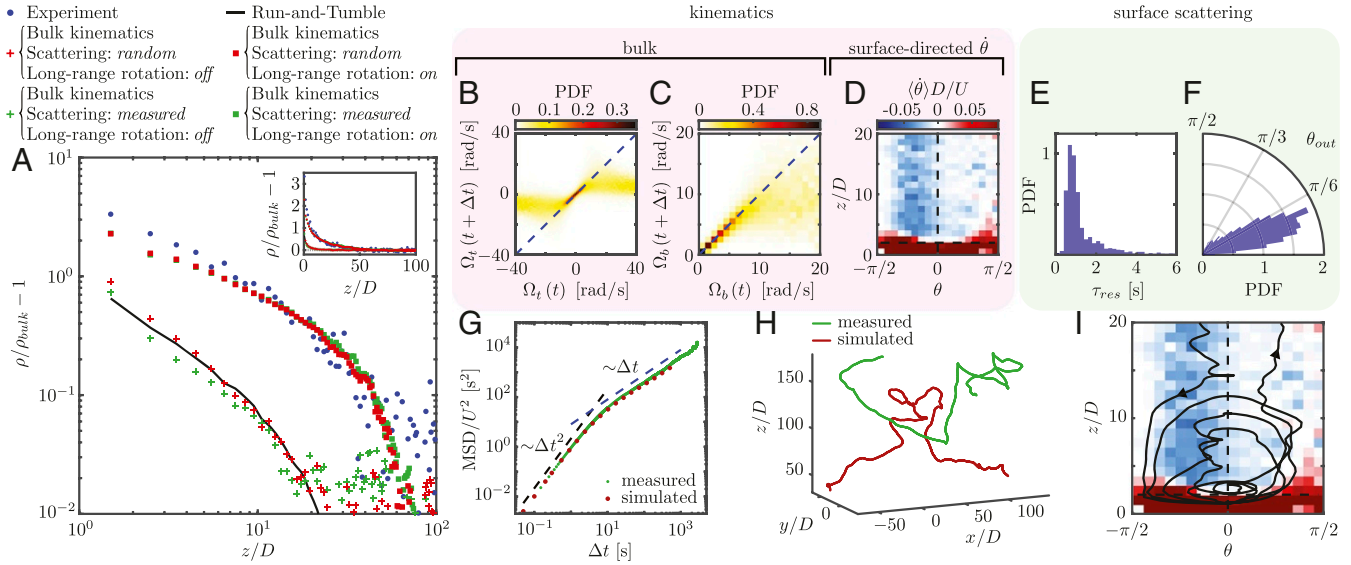

Fig. 4. (*A*) Cell density distribution along the *z* direction. Blue markers indicate the measured distribution, calculated in $\Delta z = 10$-μm bins. Red and green markers indicate the population distribution predicted via MCMC simulation. Both measured and random near-surface scattering dynamics are tested, as well as the effect of the long-range surface-directed rotation. The black line gives the expected distribution of run-and-tumble dynamics at a Péclet number, $\mathrm{Pe} = \tau U H^{-1} \approx 0.125$ with $\tau_s = 2.5$s. (*A*, *Inset*) Density distributions in linear coordinates. *B*–*F* present the probability distributions sampled in constructing the MCMC simulations. (*B* and *C*) Probability of Lagrangian rotation rate components Ω_t and Ω_b at each simulation time step, conditional on the previous value, for $\Delta t = 0.05$s. (*D*) The distribution over (θ, z) of $\dot{\theta}$. (*E* and *F*) The probability distributions describing the scattering of cells from surfaces, including residence time τ_{res} and departure angle θ_{out}. (*G*) The MSD of measured and simulated cell trajectories far from the surface ($z > 200$ μm). Each shows ballistic (MSD $\sim \Delta t^2$) behavior for $\Delta t < \tau \approx \mathcal{O}(5)$s, with diffusive behavior (MSD $\sim \Delta t$) thereafter. For clarity, only a selection of points is plotted. (*H*) Example of measured and simulated trajectories. (*I*) Near-surface hopping behavior of an example simulated trajectory.

scattering dynamics, and in particular the distinction between steric contact (10) and close-range repulsive hydrodynamic forces (19), weakly affect the cell density at the solid interface and are not responsible for the large accumulation of cells observed in our experiments of *C. reinhardtii*. Taking into account the long-range surface-directed rotation described in Fig. 3 increases the magnitude and length scale of the surface accumulation. The length scale of the resulting periodic motion toward and away from the surface sets the penetration length scale of surface accumulation of cells. Any surface topography design aimed at modulating near-surface population density in order to mediate cell-surface adhesion and subsequent biofilm growth must therefore account not only for scattering dynamics but more importantly, for long-range interactions.

Materials and Methods

Cell Culture Conditions. *C. reinhardtii* of the wild-type *CC-125* strain obtained from the *Chlamydomonas* Resource Center are maintained on solid agar slants (Alfa Aesar; H26724.22) under broad spectrum low-intensity ($\approx 30 \mu mol/m^2$s) constant illumination. From this maintenance culture, 100mL of Tris-minimal growth medium (37) was inoculated and then, exposed to a 14-h/10-h light/dark cycle ($I \approx 230 \mu mol/m^2$s) at 25°C with aeration for 4 d, by which time the culture density is $\mathcal{O}$(1e6) cells per mL and the growth is in the exponential phase. For each culture, the cells were counted using a hemocytometer (Neubauer; Marienfeld) and diluted using Tris minimal to either 2e4 or 1e5 cells per mL. This is the same protocol followed in refs. 39 and 40.

Surface Preparation. The 0.1-mm-thick glass coverslips (VWR; 631-1572), which formed the no-slip boundary with which the cells were interacting, were precleaned and treated to minimize cell-surface adhesion. They were immersed in a sonic bath in surfactant solution (Sigma-Aldrich; Z805939-1EA) for 30 min, again for 30 min in de-ionized water only, and then surface treated by immersion for > 30 min in a 1% bovine serum albumin (Sigma-Aldrich; A7906-50G) protein solution in phosphate buffer (Sigma-Aldrich; P4417-50TAB) in order to prevent cell adhesion. The coverslips were affixed to the acrylic chambers using Norland Optical Adhesive (Thorlabs; NOA81).

Cell Imaging. Excess scattered light was minimized by placing an ≈3-mm iris between the light panel and the fluidic chamber, such that only light scattered from the cells is observed by the camera sensors. The cameras do not collect direct transmitted light but only the forward scattered light at a 10° scattering angle, resulting in dark-field imaging. Swimming cells appear as individual bright spots of ≈6-pixel diameter, against a dark background.

Tracking Algorithm. Cell images were first tracked in two dimensions in each camera plane using the nearest-neighbor method, constrained to within a maximum displacement limit of 7 pixels. Corresponding tracks in other camera views were then found using an computationally efficient linear projective geometry framework through matching epipolar lines of each track projected through the other camera image planes and constrained integer assignment (46). A least squares minimization triangulated each track in physical 3D space. Track noise was eliminated via a third-order, 25-point Savitsky–Golay filter allowing higher-order kinematic derivatives, such as curvature and torsion, to be accessed analytically.

The relationship between each camera and physical space was defined using a pinhole camera model, constructed by traversing a grid pattern with regular spacing of 100μm through the measurement volume in 100-μm increments. The calibration was performed in air, and the foreshortening of the *z* coordinate due to refraction at the fluidic chamber boundaries was corrected post hoc.

Cells immobilized on the no-slip surface were identified by applying a 10-μm maximum displacement threshold over an entire temporal record. A planar estimate of the no-slip surface location was fitted to their mean position, with an offset of $\Delta z = 5 \mu m$ to account for the typical cell radius. The SD of the stationary cell locations gives the uncertainty of the estimation of the surface location as approximately $\sigma_z = 2.2 \mu m$ (*SI Appendix*, Fig. S4).

MCMC Simulations. Locations and orientations of $n_{\mathrm{cells}} \geq 10^3$ simulated cells were initialized according to a uniform distribution on $z/D \in [0, 200]$ and $\theta \in [-\pi/2, \pi/2]$. The position of each cell was computed by the time integration of the first-order dynamic $\mathbf{X}(t+\Delta t) = \mathbf{X}(t) + |\mathbf{u}_{\mathbf{cell}}| \hat{\mathbf{t}} \Delta t$, with a time step $\Delta t = 0.05s$ equal to the time resolution of the experiment and assuming $|u_{cell}| = 100 \mu$m/s. The swimming direction $\hat{\mathbf{t}}$ is stochastically updated at each time step using our experimental data. This is done by rotating the Frenet–Serret coordinate frame, $(\hat{\mathbf{t}}, \hat{\mathbf{n}}, \hat{\mathbf{b}})$, of each cell at a rotation rate sampled via the inverse transform method at each time step from the experimentally

measured rotation rate distributions. The bulk kinematics is represented by the rotation rates about the body coordinates $\hat{\mathbf{t}}$ and $\hat{\mathbf{b}}$, which were drawn from the distributions $\mathrm{P}\left(\Omega_t\left(t+\Delta t\right)|\Omega_t\left(t\right)\right)$ and $\mathrm{P}\left(\Omega_b\left(t+\Delta t\right)|\Omega_b\left(t\right)\right)$, constructed only from data recorded in the far-field region, at $z/D>50$. We verified that the distributions of these kinematic variables were statistically independent in our experiments, such that they could be sampled independently. For this, we calculated the correlation coefficients between the body-frame rotation rates both near ($z<100\ \mu m$) and far ($z>500\ \mu m$) from the surface, which were found to be close to 0: $R_{\Omega_t\Omega_b}=-0.002$ and $R_{\Omega_t\Omega_b}=-0.017$. An additional rotation, about the global coordinates, was defined by sampling $\mathrm{P}\left(\dot{\theta}\left(t\right)|\theta\left(t\right),z\left(t\right)\right)$ to model the long-range pitching dynamics.

Simulated cells were considered in contact with the surface at $z/D=1$, whereupon each was assigned a residence time and scattering angle sampled from the measured distributions, $\mathrm{P}\left(\tau_{res}\right)$ and $\mathrm{P}\left(\theta_{out}\right)$. We verified that the residence time and the scattering angle were statistically independent by computing the correlation coefficient ($R_{\tau_{\mathrm{res}}\theta_{\mathrm{out}}}=-0.059$), such that the distributions could be sampled independently. The comparison "random" scattering behavior was defined with θ_{out} uniformly distributed on $[0,\pi/2]$ and τ_{res} distributed exponentially with $\langle\tau_{res}\rangle$ equal to the diffusion timescale, τ, at $z/D>50$. The population density distribution, $\rho\left(z\right)$, was computed as the time average of the instantaneous cell locations. The residual on the population density distribution displayed first-order convergence and was $<1\%$ of ρ_{bulk} when the simulations were stopped after $\geq 10^4$ time steps (*SI Appendix*, Fig. S3).

Data Availability. Statistical distributions of the dynamics of microalgae have been deposited in 4TU.researchdata (54).

ACKNOWLEDGMENTS. This work was supported by H2020 European Research Council Grant 716712 and by Netherlands Organization for Scientific Research Project 824.15.021. We thank Da Wei and Edwin Overmars for their advice and assistance with the experiments.

1. G. D. Bixler, B. Bhushan, Biofouling: Lessons from nature. *Phil. Trans. Math. Phys. Eng. Sci.* **370**, 2381–2417 (2012).
2. R. Rusconi, R. Stocker, Microbes in flow. *Curr. Opin. Microbiol.* **25**, 1–8 (2015).
3. P. D. Frymier, R. M. Ford, H. C. Berg, P. T. Cummings, Three-dimensional tracking of motile bacteria near a solid planar surface. *Proc. Natl. Acad. Sci. U.S.A.* **92**, 6195–6199 (1995).
4. J. Elgeti, R. G. Winkler, G. Gompper, Physics of microswimmers—single particle motion and collective behavior: A review. *Rep. Prog. Phys.* **78**, 056601 (2015).
5. A. Dehkharghani, N. Waisbord, J. Dunkel, J. S. Guasto, Bacterial scattering in microfluidic crystal flows reveals giant active Taylor–Aris dispersion. *Proc. Natl. Acad. Sci. U.S.A.* **116**, 11119–11124 (2019).
6. A. Persat, H. A. Stone, Z. Gitai, The curved shape of *Caulobacter crescentus* enhances surface colonization in flow. *Nat. Commun.* **5**, 3824 (2014).
7. L. A. Pratt, R. Kolter, Genetic analysis of *Escherichia coli* biofilm formation: Roles of flagella, motility, chemotaxis and type I pili. *Mol. Microbiol.* **30**, 285–293 (1998).
8. E. Ralston, G. Swain, Bioinspiration: The solution for biofouling control? *Bioinspiration Biomimetics* **4**, 015007 (2009).
9. P. Galajda, J. Keymer, P. Chaikin, R. Austin, A wall of funnels concentrates swimming bacteria. *J. Bacteriol.* **189**, 8704–8707 (2007).
10. V. Kantsler, J. Dunkel, M. Polin, R. E. Goldstein, Ciliary contact interactions dominate surface scattering of swimming eukaryotes. *Proc. Natl. Acad. Sci. U.S.A.* **110**, 1187–1192 (2013).
11. L. Hall-Stoodley, J. W. Costerton, P. Stoodley, Bacterial biofilms: From the natural environment to infectious diseases. *Nat. Rev. Microbiol.* **2**, 95–108 (2004).
12. A. P. Berke, L. Turner, H. C. Berg, E. Lauga, Hydrodynamic attraction of swimming microorganisms by surfaces. *Phys. Rev. Lett.* **101**, 038102 (2008).
13. O. Sipos, K. Nagy, R. Di Leonardo, P. Galajda, Hydrodynamic trapping of swimming bacteria by convex walls. *Phys. Rev. Lett.* **114**, 258104 (2015).
14. G. Li, J. X. Tang, Accumulation of microswimmers near a surface mediated by collision and rotational Brownian motion. *Phys. Rev. Lett.* **103**, 078101 (2009).
15. G. Li *et al.*, Accumulation of swimming bacteria near a solid surface. *Phys. Rev. E* **84**, 041932 (2011).
16. J. Elgeti, U. B. Kaupp, G. Gompper, Hydrodynamics of sperm cells near surfaces. *Biophys. J.* **99**, 1018–1026 (2010).
17. B. Ezhilan, R. Alonso-Matilla, D. Saintillan, On the distribution and swim pressure of run-and-tumble particles in confinement. *J. Fluid Mech.* **781**, R4 (2015).
18. E. Secchi *et al.*, The effect of flow on swimming bacteria controls the initial colonization of curved surfaces. *Nat. Commun.* **11**, 2851 (2020).
19. S. E. Spagnolie, E. Lauga, Hydrodynamics of self-propulsion near a boundary: Predictions and accuracy of far-field approximations. *J. Fluid Mech.* **700**, 105–147 (2012).
20. H. Shum, E. A. Gaffney, D. J. Smith, Modelling bacterial behaviour close to a no-slip plane boundary: The influence of bacterial geometry. *Proc. Math. Phys. Eng. Sci.* **466**, 1725–1748 (2010).
21. E. Lushi, V. Kantsler, R. E. Goldstein, Scattering of biflagellate microswimmers from surfaces. *Phys. Rev.* **96**, 023102 (2017).
22. M. Mirzakhanloo, M.-R. Alam, Flow characteristics of c *Chlamydomonas* result in purely hydrodynamic scattering. *Phys. Rev. E* **98**, 012603 (2018).
23. E. Lauga, W. R. DiLuzio, G. M. Whitesides, H. A. Stone, Swimming in circles: Motion of bacteria near solid boundaries. *Biophys. J.* **90**, 400–412 (2006).
24. M. Contino, E. Lushi, I. Tuval, V. Kantsler, M. Polin, Microalgae scatter off solid surfaces by hydrodynamic and contact forces. *Phys. Rev. Lett.* **115**, 258102 (2015).
25. H. Kurtuldu, D. Tam, A. E. Hosoi, K. A. Johnson, J. P. Gollub, Flagellar waveform dynamics of freely swimming algal cells. *Phys. Rev. E* **88**, 013015 (2013).
26. B. Qin, A. Gopinath, J. Yang, J. P. Gollub, P. E. Arratia, Flagellar kinematics and swimming of algal cells in viscoelastic fluids. *Sci. Rep.* **5**, 9190 (2015).
27. H. C. Berg, How to track bacteria. *Rev. Sci. Instrum.* **42**, 868–871 (1971).
28. H. C. Berg, D. A. Brown, Chemotaxis in *Escherichia coli* analysed by three-dimensional tracking. *Nature* **239**, 500–504 (1972).
29. H. C. Crenshaw, A new look at locomotion in microorganisms: Rotating and translating. *Integr. Comp. Biol.* **36**, 608–618 (1996).
30. T.-W. Su, L. Xue, A. Ozcan, High-throughput lensfree 3D tracking of human sperms reveals rare statistics of helical trajectories. *Proc. Natl. Acad. Sci. U.S.A.* **109**, 16018–16022 (2012).
31. M. Molaei, M. Barry, R. Stocker, J. Sheng, Failed escape: Solid surfaces prevent tumbling of *Escherichia coli*. *Phys. Rev. Lett.* **113**, 068103 (2014).
32. S. J. Lee, T. Go, H. Byeon, Three-dimensional swimming motility of microorganism in the near-wall region. *Exp. Fluid* **57**, 26 (2016).
33. S. Bianchi, F. Saglimbeni, R. Di Leonardo, Holographic imaging reveals the mechanism of wall entrapment in swimming bacteria. *Phys. Rev. X* **7**, 011010 (2017).
34. S. Kim, S. J. Lee, Effect of particle number density in in-line digital holographic particle velocimetry. *Exp. Fluid* **44**, 623–631 (2008).
35. P. Memmolo *et al.*, Recent advances in holographic 3D particle tracking. *Adv. Opt. Photon* **7**, 713–755 (2015).
36. J. Gao, D. R. Guildenbecher, P. L. Reu, J. Chen, Uncertainty characterization of particle depth measurement using digital in-line holography and the hybrid method. *Opt. Express* **21**, 26432–26449 (2013).
37. E. H. Harris, D. B. Stern, G. B. Witman, *The Chlamydomonas Sourcebook* (Academic Press, London, United Kingdom, ed. 2, 2009).
38. K. Drescher, R. E. Goldstein, N. Michel, M. Polin, I. Tuval, Direct measurement of the flow field around swimming microorganisms. *Phys. Rev. Lett.* **105**, 168101 (2010).
39. G. Quaranta, M.-E. Aubin-Tam, D. Tam, Hydrodynamics versus intracellular coupling in the synchronization of eukaryotic flagella. *Phys. Rev. Lett.* **115**, 238101 (2015).
40. D. Wei, P. G. Dehnavi, M.-E. Aubin-Tam, D. Tam, Is the zero Reynolds number approximation valid for ciliary flows? *Phys. Rev. Lett.* **122**, 124502 (2019).
41. K. W. Foster, R. D. Smyth, Light antennas in phototactic algae. *Microbiol. Rev.* **44**, 572–630 (1980).
42. K. W. Foster *et al.*, A rhodopsin is the functional photoreceptor for phototaxis in the unicellular eukaryote *Chlamydomonas*. *Nature* **311**, 756–759 (1984).
43. T. Takahashi, M. Watanabe, Photosynthesis modulates the sign of phototaxis of wild-type *Chlamydomonas reinhardtii*. *FEBS. Lett.* **336**, 516–520 (1993).
44. H. Kim, S. Große, G. E. Elsinga, J. Westerweel, Full 3d-3c velocity measurement inside a liquid immersion droplet. *Exp. Fluid* **51**, 395–405 (2011).
45. H. Kim, J. Westerweel, G. E. Elsinga, Comparison of tomo-PIV and 3d-PTV for microfluidic flows. *Meas. Sci. Technol.* **24**, 024007 (2012).
46. A. Attanasi *et al.*, Greta-a novel global and recursive tracking algorithm in three dimensions. *IEEE Trans. Pattern Anal. Mach. Intell.* **37**, 2451–2463 (2015).
47. K. Muller, C. K. Hemelrijk, J. Westerweel, D. S. W. Tam, Calibration of multiple cameras for large-scale experiments using a freely moving calibration target. *Exp. Fluid* **61**, 7 (2020).
48. K.-T. Wu, Y.-T. Hsiao, W.-Y. Woon, Entrapment of pusher and puller bacteria near a solid surface. *Phys. Rev.* **98**, 052407 (2018).
49. J. E. Gentle, *Random Number Generation and Monte Carlo Methods* (Springer-Verlag, New York, NY, ed. 2, 2003).
50. M. Polin, I. Tuval, K. Drescher, J. P. Gollub, R. E. Goldstein, *Chlamydomonas* swims with two "gears" in a eukaryotic version of run-and-tumble locomotion. *Science* **325**, 487–490 (2009).
51. Y. Or, S. Zhang, R. Murray, Dynamics and stability of low-Reynolds-number swimming near a wall. *SIAM J. Appl. Dyn. Syst.* **10**, 1013–1041 (2011).
52. K. Ishimoto, E. A. Gaffney, Squirmer dynamics near a boundary. *Phys. Rev. E* **88**, 062702 (2013).
53. S. Yazdi, A. M. Ardekani, A. Borhan, Swimming dynamics near a wall in a weakly elastic fluid. *J. Nonlinear Sci.* **25**, 1153–1167 (2015).
54. A.-J. Buchner, K. Muller, J. Mehmood, D. Tam, Statistics of the kinematics of free-swimming microalgae. 4TU.ResearchData. https://doi.org/10.4121/14501823. Deposited 30 April 2021.